Prediction of exotic magnetic states in the alkali-metal quasi-one-dimensional iron selenide compound Na₂FeSe₂

Bradraj Pandey [1,3] Ling-Fang Lin [1,2] Rahul Soni [1,3] Nitin Kaushal,[1,3] Jacek Herbrych,[4] Gonzalo Alvarez,[5] and Elbio Dagotto[1,3]

[1]*Department of Physics and Astronomy, University of Tennessee, Knoxville, Tennessee 37996, USA*
[2]*School of Physics, Southeast University, Nanjing 211189, China*
[3]*Materials Science and Technology Division, Oak Ridge National Laboratory, Oak Ridge, Tennessee 37831, USA*
[4]*Department of Theoretical Physics, Faculty of Fundamental Problems of Technology,
Wroclaw University of Science and Technology, 50-370 Wroclaw, Poland*
[5]*Computational Sciences & Engineering Division and Center for Nanophase Materials Sciences,
Oak Ridge National Laboratory, Oak Ridge, Tennessee 37831, USA*

The magnetic and electronic phase diagram of a model for the quasi-one-dimensional alkali-metal iron selenide compound Na₂FeSe₂ is presented. The novelty of this material is that the valence of iron is Fe^{2+}, contrary to most other iron-chain compounds with valence Fe^{3+}. Using first-principles techniques, we developed a three-orbital tight-binding model that reproduces the *ab initio* band structure near the Fermi level. Including Hubbard and Hund couplings and studying the model via the density-matrix renormalization group and Lanczos methods, we constructed the ground-state phase diagram. A robust region where the block state ↑↑↓↓↑↑↓↓ is stabilized was unveiled. The analog state in iron ladders, employing 2×2 ferromagnetic blocks, is by now well established, but in chains a block magnetic order has not been observed yet in real materials. The phase diagram also contains a large region of canonical staggered spin order ↑↓↑↓↑↓↑↓ at very large Hubbard repulsion. At the block-to-staggered transition region, an exotic phase is stabilized with a mixture of both states: an inhomogeneous orbital-selective charge density wave with the exotic spin configuration ↑↑↓↑↓↓↑↓. Our predictions for Na₂FeSe₂ may guide crystal growers and neutron-scattering experimentalists towards the realization of block states in one-dimensional iron selenide chain materials.

I. INTRODUCTION

Iron-based pnictides and selenides are fascinating materials with exotic magnetic and superconducting properties [1–3]. For iron selenides the low-temperature insulating ground state has robust local magnetic moments [4–6], highlighting the importance of Hubbard and Hund coupling interactions among the electrons occupying the $3d$ orbitals [2,3]. The competition between charge, spin, lattice, and orbital degrees of freedom can give rise to various types of exotic magnetic and electronic ordering. In particular, recently the two-leg ladder iron selenide materials have received considerable attention. One reason is their similarity with copper-based ladders, with a spin gap in the undoped limit and superconductivity upon doping by high pressure [7,8]. Moreover, in the two-leg ladder iron-based compound BaFe₂Se₃, an exotic block-antiferromagnetic (AFM) order (involving 2×2 ferromagnetically aligned blocks, coupled antiferromagnetically along the legs of the ladder) has been reported using inelastic neutron-diffraction methods [9–13], confirming earlier predictions by theory [14,15]. BaFe₂Se₃ is an insulator with robust Néel temperature $T_N \sim 250$ K into the block phase and large individual magnetic moments $\sim 2.8\mu_B$. In another iron-based ladder material, where K replaces Ba leading to KFe₂Se₃, the magnetic moments align ferromag-

netically along the rungs but antiferromagnetically along the legs forming 2×1 blocks [10].

In addition to these ladder materials, there are some experimentally observed iron selenide compounds, such as TlFeS₂, TlFeSe₂, and KFeSe₂, which contain weakly coupled quasi-one-dimensional *chains* [16,17]. In these compounds iron is in a valence Fe^{3+}, corresponding to $n = 5$ electrons in the $3d$ iron orbitals. Based on magnetic susceptibility, electric resistivity, and electron-spin resonance, TlFeSe₂ behaves as a quasi-one-dimensional standard spin-staggered antiferromagnet [18]. Furthermore, neutron-diffraction experiments on TlFeS₂ also indicate [19] staggered spin order below $T_N = 196$ K.

The experimental developments described above in quasi-1D iron-based materials provides a playground for theoretical many-body calculations based on the multiorbital Hubbard model [20–24]. Using accurate numerical techniques for low-dimensional systems, such as the density-matrix renormalization group method (DMRG) [25,26], the high-pressure superconducting two-leg ladder compound BaFe₂S₃ [27–29] was explored with regards to magnetic and pairing properties keeping two orbitals active [30,31]. Evidence for the correct rung-FM and leg-AFM spin order was found over large portions of interaction parameters [30]. Evidence of metallization under high pressure was also reported [32,33]. This is

considered a precursor of superconductivity, which was also shown to appear in theoretical studies of two-orbital one-dimensional models upon hole doping [20,21]. Even multiferroicity was unveiled in iron ladders [34], indicating an unexpected rich behavior. Moreover, novel Te-based ladders were predicted to display interesting magnetic properties as well [35,36].

The phase diagram of a three-orbital Hubbard model for chains was also studied using DMRG [14,15], unveiling various types of exotic magnetic and electronic phases. More canonical ferromagnetic and staggered $\uparrow\downarrow\uparrow\downarrow$ states were also stabilized, varying the Hund and Hubbard interaction parameters. The spin dynamical properties of exotic orbital-selective Mott phases (displaying the selective localization of electrons on a particular orbital) were also analyzed, revealing unusual coexisting modes of spin excitations [23].

The magnetic phase diagram of the five-orbital Hubbard model for iron selenide materials was initially studied using real-space Hartree-Fock approximations for chains [37] and ladders [38]. At electronic density $n = 5$, relevant to previously known chain compounds such as TlFeSe$_2$, a simple staggered AFM phase in a large parameter space of the phase diagram was reported, in agreement with existing experiments. Interestingly, a much richer phase diagram was theoretically predicted for chains with the electronic density $n = 6$. More reliable DMRG studies of the three-orbital Hubbard model at $n = 6$ have also consistently reported a similar wide variety of exotic phases for $n = 6$, including the block phase $\uparrow\uparrow\downarrow\downarrow$ at robust Hund coupling [14], as well as generalizations to longer blocks [22] and even spontaneously formed spiral phases [39]. But thus far only two-leg ladder materials, such as BaFe$_2$Se$_3$ and BaFe$_2$S$_3$, have been studied experimentally, confirming the block nature of the spin state—either 2×2 or 2×1 blocks—as well as exotic superconductivity upon high pressure. However, finding a truly $n = 6$ one-dimensional version, with only chains instead of ladders, would add another interesting member to the existing group of realizations of the theory predictions, opening a novel avenue for research.

Recently, the possibility of preparing the alkali iron selenide compound Na$_2$FeSe$_2$ has been discussed [40]. In Na$_2$FeSe$_2$ the iron atom is in a valence state Fe^{2+}, which corresponds to an electronic density $n = 6$ for the 3d Fe orbitals. As already discussed, Hartree-Fock studies of low-dimensional multiorbital models with electronic density $n = 6$ displayed a much richer phase diagram with exotic phases as compared to the canonical staggered order of the $n = 5$ case. Motivated by recent experimental efforts [40], in this publication we study theoretically the magnetic and electronic properties of the chain compound Na$_2$FeSe$_2$. Using first-principles calculations we obtain the relevant hopping amplitudes. Next, using computationally accurate techniques such as DMRG and Lanczos methods, we construct the ground-state phase diagram by varying the on-site same-orbital Hubbard U repulsion and the on-site Hund coupling J_H. At low values of J_H/U, the staggered AFM order with wave vector π dominates in a large portion of the phase diagram. However, upon increasing J_H/U into the realistic regime for iron-based compounds, interesting block phases, particularly $\uparrow\uparrow\downarrow\downarrow$, dominate in a large region of parameter space. In contrast to Hartree-Fock methods, DMRG and Lanczos take into account quantum fluc-

FIG. 1. (a) Crystal structure of Na$_2$FeSe$_2$, the material that we predict should present exotic magnetic order. (b) Side view of a single Fe chain and the nearest-neighbor t and next-nearest-neighbor t' hopping amplitudes used in our study. The dashed line indicates the primitive unit cell used in DFT calculations.

tuations, rendering the results more reliable. Finally, albeit in a narrow region of parameter space, a novel phase $\uparrow\uparrow\downarrow\uparrow\downarrow\downarrow\uparrow\downarrow$ was also found with a mixture of properties of the dominant block and staggered states.

The organization of the paper is as follows. In Sec. II, details of the *ab initio* calculations are described. Section III contains the three-orbital Hubbard model and details of the numerical methods. Section IV presents the DMRG and Lanczos predictions, where first we focus on the results at the realistic Hund coupling $J_H/U = 1/4$, and later an extended phase diagram of the model is provided. Finally, conclusions are provided in Sec. V.

II. *AB INITIO* CALCULATIONS

The crystal structure of Na$_2$FeSe$_2$ is shown in Fig. 1. The most prominent feature is that edge-sharing FeSe$_2$ tetrahedral forming one-dimensional chains running along the c axis. Here, first-principles density functional theory (DFT) calculations are used, employing the lattice constants a, b, and c, and the atomic positions of the Na, Fe, and Se atoms as reported in Ref. [40]. These lattice constants are $a = 6.608$ Å, $b = 11.903$ Å, and $c = 5.856$ Å. The space group is *Ibam* (no. 72), and the atomic positions of Na(8j), Fe(4a), and Se(8j) are (0.1562, 0.35565, 0.0), (0.0, 0.0, 0.25), and (0.21638, 0.11435, 0.0), respectively. The band structure and the projected density of states for the 3d orbitals are presented in Figs. 2(a) and 2(b). The orbital $d_{x^2-y^2}$ contributes primarily
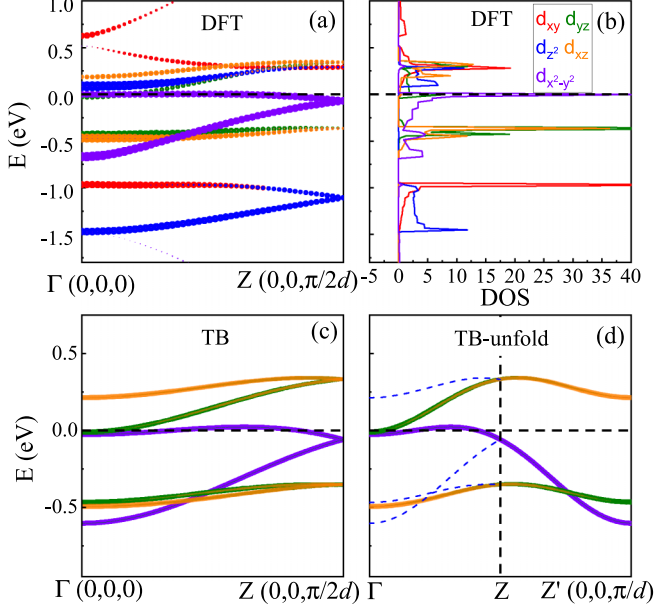
FIG. 2. (a) Band structure and (b) projected density of states of the Na_2FeSe_2 single-chain compound obtained using DFT calculations. (c) Tight-binding (TB) band structure in the folded zone. (d) Tight-binding unfolded (TB-unfold) band structure used in the DMRG calculations. Parts of the original folded bands are marked with blue dashed lines. The zero in the vertical energy axis is the position of the Fermi level.

near the Fermi level. The contribution of the orbitals d_{xz} and d_{yz} is subdominant but not negligible.

Considering the one-dimensional character of the atomic structure, all interchain electron hopping amplitudes are neglected and we only focus on the intrachain hoppings. In other words, only a Na_2FeSe_2 single chain [shown in Fig. 1(b)] is considered in the DFT procedure. The calculations were performed using the generalized gradient approximation [41] and the projector augmented wave (PAW) pseudopotentials [42], implemented in the Vienna *ab initio* Simulation Package (VASP) code [43,44]. Since the magnetic properties will be considered via many-body calculations, magnetism was not included in the derivation of the bands and hopping amplitudes from first principles. Following a self-consistent calculation with total energy convergence of order 10^{-5} eV, the maximally localized Wannier functions [45] were constructed using the WANNIER90 code [46] from the *ab initio* ground-state wave function.

We constructed three Wannier functions involving the orbital basis d_{xz}, d_{yz}, $d_{x^2-y^2}$ for each iron and deduced the hopping parameters, readjusted to properly fit the band structure after reducing the original five orbitals to three (see Sec. III for details). The corresponding band structure using these hoppings is displayed in Fig. 2(c), which agrees well with the DFT band structure. Note that there are two Fe atoms in the primitive unit cell in the DFT calculation because of the alternating positions of the Na and Se atoms, leading to a unit cell of $2d$ length, where d is the distance between two nearest-neighbor iron atoms [see Fig. 1(b)]. Therefore the corresponding band structure can be described as a six-band

model, i.e., three orbitals for two iron atoms in the primitive unit cell. Since we focus only on the iron atoms (as discussed previously for other iron-based compounds in Refs. [47,48]), we can exclude the Na and Se atoms, which further simplifies the primitive unit cell. By including only one iron atom in the primitive unit cell, the lattice constant of the new unit cell is called d. In other words, by introducing a local gauge transformation for one of the two orbitals to change its sign, we can expand the band dispersion from Γ-Z to Γ-Z′, as shown in Fig. 2(d). As a result, the band structure can be unfolded and simplified to a three-band model that was used in the DMRG calculations.

III. MODEL AND METHOD

The Hamiltonian for the one-dimensional chain of Na_2FeSe_2, with three orbitals at each iron site, will be described by the multiorbital Hubbard $H = H_k + H_{in}$. The kinetic or tight-binding component contains the nearest- and next-nearest-neighbor hopping:

$$H_k = \sum_{i,\sigma,\gamma,\gamma'} t_{\gamma,\gamma'}(c^{\dagger}_{i\sigma,\gamma}c_{i+1,\sigma,\gamma'} + \text{H.c.})$$
$$+ t'_{\gamma,\gamma'}(c^{\dagger}_{i\sigma,\gamma}c_{i+2,\sigma,\gamma'} + \text{H.c.}) + \sum_{i\gamma\sigma}\Delta_{\gamma}n_{i,\sigma\gamma}, \quad (1)$$

where $t_{\gamma,\gamma'}$ is the nearest-neighbor (NN) 3×3 hopping amplitude matrix between sites i and $i + 1$ in the orbital space $\gamma = \{d_{xz}, d_{yz}, d_{x^2-y^2}\}$. $n_{i,\sigma\gamma}$ stands for the orbital- and spin-resolved particle number operator. These orbitals will be referred to as $\gamma = \{1, 2, 3\}$, respectively, in the remainder of the paper, for notation simplicity. As explained before, the hopping matrices for Na_2FeSe_2 were obtained from a tight-binding Wannier function analysis of first-principles results and they are in electronvolt units. Explicitly, the NN 3×3 matrix $t_{\gamma,\gamma'}$ between sites i and $i + 1$ in orbital space is given by

$$t_{\gamma,\gamma'} = \begin{bmatrix} -0.177 & 0.171 & 0.000 \\ -0.171 & 0.114 & 0.000 \\ 0.000 & 0.000 & 0.144 \end{bmatrix},$$

where γ are the orbitals for site i and γ' for site $i + 1$. $t'_{\gamma,\gamma'}$ is the next-nearest-neighbor (NNN) hopping matrix between sites i and $i + 2$:

$$t'_{\gamma,\gamma'} = \begin{bmatrix} -0.037 & -0.003 & 0.000 \\ 0.003 & -0.053 & 0.000 \\ 0.000 & 0.000 & -0.064 \end{bmatrix}.$$

The on-site matrix containing the crystal fields Δ_{γ} for each orbital is given by

$$t^{OnSite}_{\gamma,\gamma} = \begin{bmatrix} -0.068 & 0.000 & 0.000 \\ 0.000 & -0.134 & 0.000 \\ 0.000 & 0.000 & -0.188 \end{bmatrix}.$$

Note that we follow the convention that each 3×3 matrix (both $t_{\gamma,\gamma'}$ and $t'_{\gamma,\gamma'}$) represents the hopping matrix to move from one iron site to another. The full hopping matrix, which includes both the back-and-forth hopping processes, are of size 6×6 containing $t_{\gamma,\gamma'}$ in the upper off-diagonal block,

the transpose of $t_{\gamma,\gamma'}$ in the lower off-diagonal block, and the on-site matrix $t_{\gamma,\gamma}^{\mathrm{OnSite}}$ in both diagonal blocks [38]. The kinetic energy bandwidth is $W = 0.94$ eV.

The electronic interactions portion of the Hamiltonian is standard:

$$H_{\mathrm{in}} = U \sum_{i\gamma} n_{i\uparrow\gamma} n_{i\downarrow\gamma} + \left(U' - \frac{J_H}{2} \right) \sum_{i,\gamma<\gamma'} n_{i\gamma} n_{i\gamma'}$$
$$- 2J_H \sum_{i,\gamma<\gamma'} \mathbf{S}_{i,\gamma} \cdot \mathbf{S}_{i,\gamma'} + J_H \sum_{i,\gamma<\gamma'} (P_{i\gamma}^+ P_{i\gamma'} + \mathrm{H.c.}).$$

(2)

The first term is the Hubbard repulsion between electrons in the same orbital. The second term is the electronic repulsion between electrons at different orbitals where the standard relation $U' = U - 2J_H$ is assumed. The third term represents the Hund's interaction between electrons occupying the active $3d$ orbitals. The operator $\mathbf{S}_{i,\gamma}$ is the total spin at site i and orbital γ. The fourth term is the pair hopping between different orbitals at the same site i, where $P_{i,\gamma} = c_{i\downarrow\gamma} c_{i\uparrow\gamma}$.

To solve numerically this Hamiltonian and obtain the ground-state properties of Na_2FeSe_2, the DMRG and Lanczos methods were used. Open boundary conditions were employed in DMRG and at least 1200 states kept during the calculations. For these DMRG calculations, we used the DMRG++ computer program [49]. We fixed the electronic density per orbital to be $n = 4/3$ (four electrons per site, i.e., four electrons in three orbitals). Such electronic density is used in the context of iron superconductors where iron is in a valence Fe^{2+}, corresponding to six electrons in five orbitals. A common simplification is to drop one orbital doubly occupied and one empty, leading to four electrons in the remaining three orbitals. Most of the DMRG calculations were performed using chains of length $L = 16$ and $L = 24$, which for our purposes of finding the magnetic properties of the ground state are sufficient. Furthermore, by investigating small lattice sizes ($L = 4$) with exact Lanczos diagonalization we reached the same conclusions.

IV. RESULTS

In Fig. 3, we show the phase diagram of the three-orbital Hubbard model. We use realistic *ab initio* hopping amplitudes for Na_2FeSe_2 and vary U/W at fixed Hund coupling $J_H/U = 1/4$ [50]. This phase diagram was constructed based on DMRG calculations measuring several observables: the site-average electronic density at each orbital $n_\gamma = \frac{1}{L} \sum_{i,\sigma} \langle n_{i\sigma\gamma} \rangle$, the spin-spin correlation $S(r) = \langle \mathbf{S}_m \cdot \mathbf{S}_l \rangle$ (where $r = |m - l|$; m and l are sites), and the spin structure factor $S(q) = \frac{1}{L} \sum_{m,l} e^{-iq(m-l)} \langle \mathbf{S}_m \cdot \mathbf{S}_l \rangle$ using primarily a system size $L = 16$. The global electronic density is $n = 4/3$ (four electrons in three orbitals at each site in average).

Four different phases were found: (i) a paramagnetic phase (PM) at small U/W, followed by (ii) an unexpected block phase (AF2) where ferromagnetic clusters of two spins are coupled antiferromagnetically in a ↑↑↓↓ pattern. Then (iii) an intermediate electronically inhomogeneous and spin exotic state (AF3) was found, with ferro- and antiferromagnetic ordering ↑↑↓↑↓↓↑↓. Finally, (iv) a canonical staggered antiferromagnetic phase (AF1) ↑↓↑↓ becomes stable. To
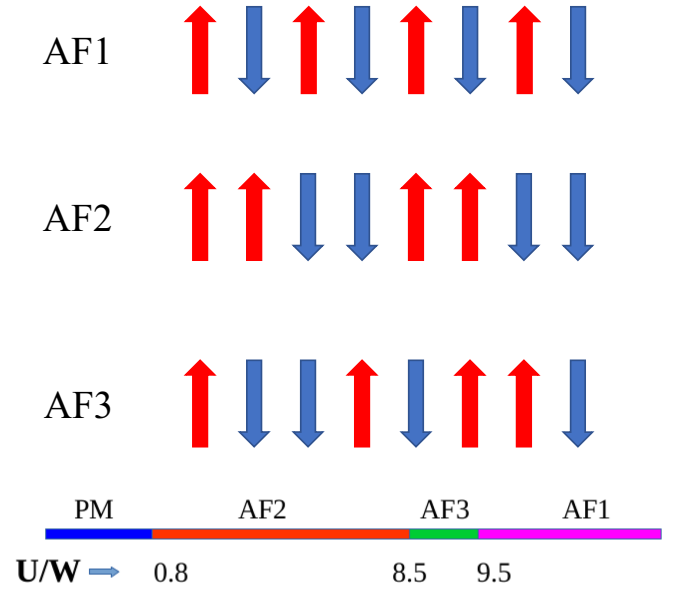
FIG. 3. Schematic representation of the magnetic states observed in the phase diagram. (i) AF1: standard staggered antiferromagnetic phase ↑↓↑↓; (ii) AF2: antiferromagnetically coupled ferromagnetic blocks resulting in ↑↑↓↓ spin order. (iii) AF3: mixed ferro- and antiferromagnetic ordering ↑↑↓↑↓↓↑↓ stable in a narrow region of couplings. At the bottom: schematic phase diagram of the ground state for fixed $J_H/U = 0.25$.

distinguish among these magnetic phases and to obtain the approximate phase boundary location, we studied $S(q_p)$ vs U/W, where $q = q_p$ is defined as the wave vector that displays a sharp peak for each value of U/W studied.

A. Results at Hund coupling $J_H/U = 1/4$

1. (a) AF2 and AF1 phases

At small Hubbard interaction U/W the system displays metallic behavior without any dominant magnetic order, as expected. In this PM regime, the spin correlation $S(r)$ decays rapidly with distance in the range $U/W < 0.8$, as exemplified in Fig. 4(a). Increasing the Hubbard interaction U/W, the system enters into the block phase with AF2 magnetic ordering. In Fig. 4(b), the spin correlations $S(r)$ at $U/W = 4.0$ are presented, clearly showing the formation of antiferromagnetically coupled ferromagnetic spin clusters in a ↑↑↓↓ pattern. Because of this block order, the spin structure factor $S(q)$ in the AF2 phase displays a sharp peak at $q = \pi/2$, shown in Fig. 4(d). The peak value increases with the system size L, providing evidence of a stable, exotic $\pi/2$-block magnetic state in the system. Note that the canonical power-law decaying real-space correlations in one dimension prevents $S(q)$ from diverging with increasing L, but in a real material it is expected that weak interchain couplings will stabilize the several phases we have observed.

As shown in Fig. 5(a), $S(q_p) = S(\pi/2)$ dominates in the range $0.8 \lesssim U/W \lesssim 8.5$, signalling a stable block phase in a broad region of parameter space at $J_H/U = 0.25$. Similar block AF2 spin patterns, albeit extended in two dimensions into 2×2 ferromagnetic blocks, have been also experimentally observed in two-dimensional
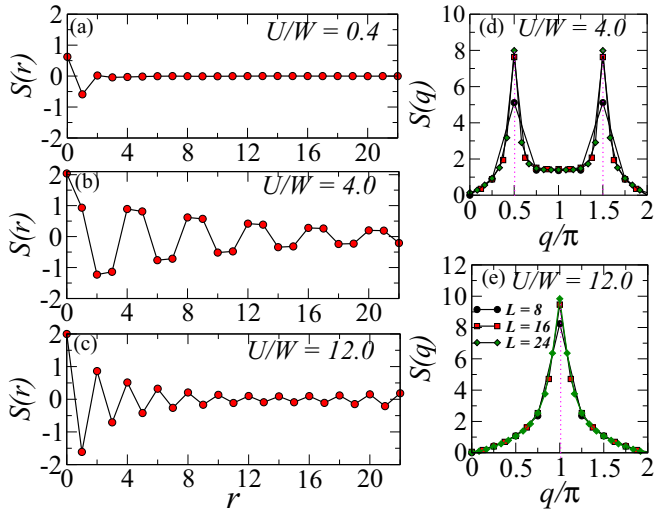
FIG. 4. Real-space spin correlation $S(r) = \langle \mathbf{S}_m \cdot \mathbf{S}_l \rangle$, with $r = |m - l|$, for various values of the Hubbard interaction U/W, at fixed $J_H/U = 0.25$ and using an $L = 24$ cluster studied with DMRG. Results are shown for (a) the PM phase at $U/W = 0.4$, (b) the block phase (AF2) at $U/W = 4.0$, and (c) the staggered AF1 phase at $U/W = 12.0$. The AF3 state will be discussed later in Fig. 6. The spin structure factor $S(q)$ is shown for three values of L at (d) $U/W = 4.0$ in the block AF2 phase and (e) $U/W = 12.0$ in the AF1 phase.

iron-selenium–based compounds with vacancies, such as $Rb_{0.89}Fe_{1.58}Se_2$ and $K_{0.8}Fe_{1.6}Se_2$ [6], and more importantly for our purposes, also in the two-leg ladder $BaFe_2Se_3$ [9], which is a close "relative" of the Na_2FeSe_2 compound due to the common one dimensionality and iron valence Fe^{2+}. Although it is difficult to establish with clarity what induces
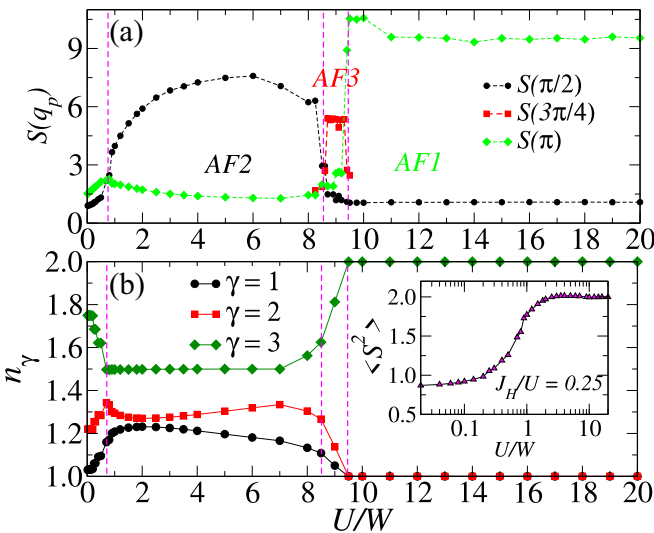
FIG. 5. (a) Spin structure factor $S(q_p)$ vs U/W at $J_H/U = 0.25$ for several values of the three dominant wave vectors shown in the legend. (b) Site-average electronic occupancy n_γ for the three orbitals $\{\gamma = 1, 2, 3\}$ vs U/W using DMRG and a chain of $L = 16$ sites. Inset: Site-average expectation value of the total spin squared vs U/W at $J_H/U = 0.25$.

this block state, previous work [14] suggests that this phase is a result of competition between the Hund coupling J_H, favoring ferromagnetic alignment of spins as in double-exchange manganites [51], and the standard superexchange Hubbard spin-spin interaction that aligns the spins antiferromagnetically. One surprising aspect is that in the block AF2 phase the population of orbital $\gamma = 3$ appears locked to 1.5 in all the range of U/W investigated [Fig. 5(b)]. On the other hand, the occupancies of the other orbitals $\gamma = 1$ and $\gamma = 2$ change with varying U/W in the same range.

In the inset of Fig. 5(b), the mean value of the local spin-squared averaged over all sites $\langle S^2 \rangle = \frac{1}{L} \sum_i \langle \mathbf{S}_i \cdot \mathbf{S}_i \rangle$ is shown vs U/W. For $U/W > 1.0$, strong local magnetic moments are fully developed at every site with spin magnitude $S \approx 1$, as expected for four electrons in three orbitals and a robust Hund coupling. In experiments, alkali-metal iron selenide compounds generally show large magnetic moments, particularly when compared to iron pnictide compounds.

In Fig. 5(b), the site-average occupancy of orbitals n_γ vs U/W is shown, and for $U/W > 9.5$ the population of orbital $\gamma = 3$ reaches 2, thus decoupling from the system, while the other two orbitals $\gamma = 1, 2$ reach population 1. This arrangement minimizes the double occupancy at large U/W. In this Mott AF1 phase, the spin correlations show a canonical staggered AFM ordering, see Fig. 4(c), due to the dominating effect of the superexchange mechanism in the system, now involving only two active orbitals. The structure factor displays a sharp peak at $q = \pi$, see Fig. 4(e).

2. Inhomogeneous AF3 phase

At interaction $8.5 < U/W < 9.5$, a novel orbital-selective charge density wave phase was observed with an exotic AF3 spin ordering. This phase exists for all the lattice sizes analyzed, and moreover, it appears using both DMRG and Lanczos, as shown below; thus we believe it is a real regime of the present model. Figure 6(a) displays the population of the three orbitals $\langle n_{\gamma,i} \rangle$ vs the site index i at $U/W = 9.1$. The results show an orbital-selective charge density wave phase. The pattern that develops has two sites with integer fillings, such as 1.0 and 2.0, followed by two sites with a fractional filling for all three orbitals. Orbital 3 jumps from population 2.0 as in the AF1 phase, to population 1.5 as in the AF2 phase, as compared with Fig. 5(b). The other two orbitals 1 and 2 display similar characteristics, namely, a mixture of AF1 and AF2 features.

Interestingly, in parallel to an inhomogeneous charge density arrangement, a novel spin pattern AF3 $\uparrow\uparrow\downarrow\uparrow\uparrow\downarrow\downarrow\uparrow\downarrow$ develops in the system for this range of U/W, see Fig. 6(b). The structure factor $S(q)$ shows a peak at $q = 3\pi/4$ which grows with increasing the system size, see Fig. 6(c). The phase boundary of this exotic AF3 phase is determined by comparing the peaks of the spin structure factors. As shown in Fig. 5(b), the peak at $q = 3\pi/4$ clearly dominates over other peaks of $S(q)$ in the range $8.5 < U/W < 9.4$. Similar spin configurations have also been reported in the study of the one-dimensional two-orbital Hubbard model [22] at density $n = 2.33$. We believe that this exotic phase stabilizes in the phase diagram, mainly due to the NNN hopping $t'_{\gamma,\gamma'}$, since it generates frustration in the system. Eventually, for large enough values of the Hubbard interaction $U/W > 9.5$,
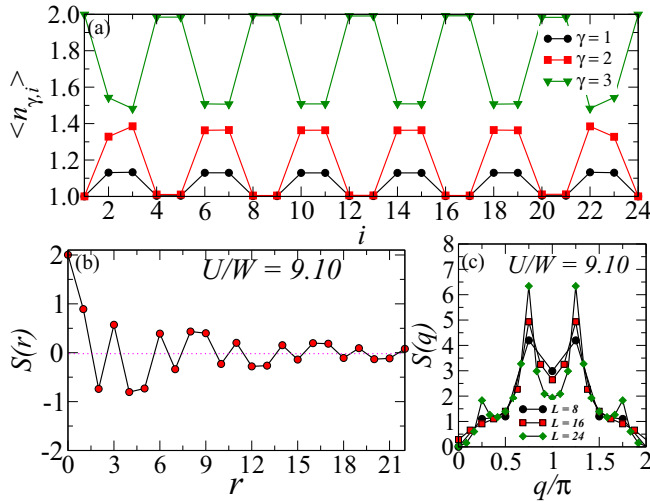
FIG. 6. (a) Electronic occupancy $\langle n_{\gamma,i} \rangle$ for the three orbitals $\{\gamma = 1, 2, 3\}$ vs site index i at $U/W = 9.1$, $L = 24$, in the AF3 regime showing an orbital-selective charge density wave. (b) Spin correlation $S(r) = \langle \mathbf{S}_m \cdot \mathbf{S}_l \rangle$ at $U/W = 9.1$ using a $L = 24$ cluster displaying the AF3 magnetic ordering $\uparrow\uparrow\downarrow\uparrow\uparrow\downarrow\downarrow\uparrow\downarrow$. (c) The spin structure factor for three different values of $L = 8, 16, 24$ and at $U/W = 9.1$. Clear peaks at $q = 3\pi/4$ are shown.

the system enters into the insulating Mott phase with staggered AF1 magnetic ordering.

3. Density of states and charge fluctuations

To characterize, at least qualitatively, the metallic vs insulating nature of the different phases, we have calculated the orbital-resolved density of states using the Lanczos method for small $L = 4$ three-orbital Hubbard model clusters. While these clusters are small, the results are exact. Figure 7 contains the orbital-resolved density of states (DOS) vs $\omega - \mu$ (ω is the frequency and μ the chemical potential) for different values of the interaction parameter U/W. In the paramagnetic phase, all three orbitals have a robust weight at the Fermi level, Fig. 7(a), indicating metallic behavior. For the block phase at $U/W = 4$, we observe considerably lower weight at the Fermi level for all three orbitals, Fig. 7(b), signaling a possible pseudogap and bad metallic behavior in the system. As expected, in the Mott phase Fig. 7(c) shows that at $U/W = 10$ the system opens a large gap, confirming the insulating nature of the AF1 state. The lower Hubbard band of insulating orbitals 1 and 2 is not shown (located much lower in energy).

To better understand the characteristics of metallic vs insulating behavior, in addition to Lanczos we have calculated the orbital-resolved local density of state $\rho_{i,\gamma}(\omega)$ as a function of frequency ω using dynamical DMRG within the correction-vector formalism in Krylov space [52]. The orbital-resolved local density of state (LDOS) has two components: (i) Above the chemical potential it becomes

$$\rho_{i,\gamma}^{+}(\omega) = \frac{-1}{\pi} Im\left[\langle \psi_0 | c_{i,\gamma} \frac{1}{\omega - H + E_g + i\eta} c_{i,\gamma}^{\dagger} | \psi_0 \rangle \right], \quad (3)$$

and (ii) below the chemical potential the LDOS is

$$\rho_{i,\gamma}^{-}(\omega) = \frac{1}{\pi} Im\left[\langle \psi_0 | c_{i,\gamma}^{\dagger} \frac{1}{\omega + H - E_g - i\eta} c_{i,\gamma} | \psi_0 \rangle \right], \quad (4)$$
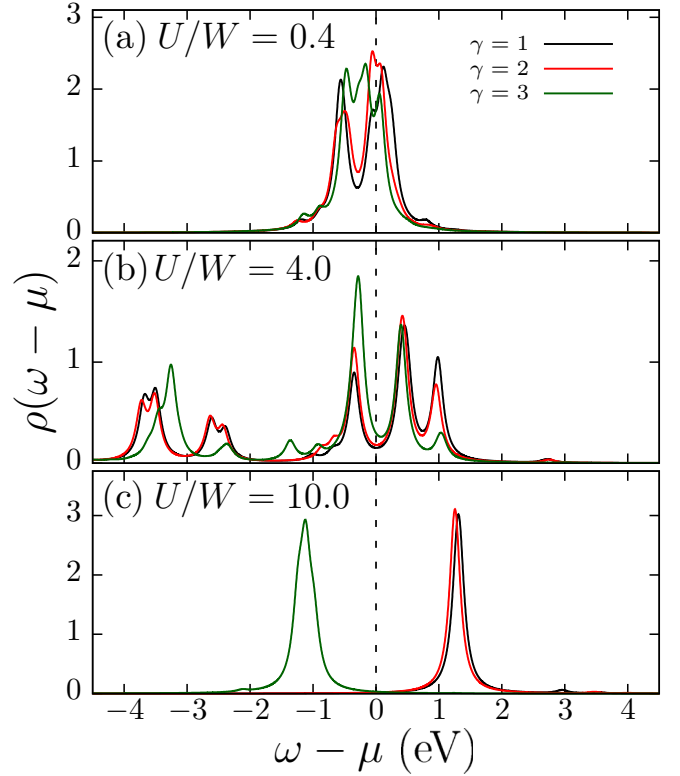
FIG. 7. DOS of different orbitals corresponding to different phases at $J_H/U = 0.25$ on a four-site three-orbital system using Lanczos diagonalization. (a) Corresponds to the PM phase at $U/W = 0.4$, (b) is for the AF2 phase at $U/W = 4.0$, while (c) is for the AF1 phase at $U/W = 10.0$.

where $c_{i,\gamma}$ is the fermionic annihilation operator while $c_{i,\gamma}^{\dagger}$ is the creation operator, E_g is the ground-state energy, and ψ_0 is the ground-state wave function of the system. We set the broadening parameter as $\eta = 0.1$ for the DMRG calculations. To avoid edge effects, for the LDOS we chose a central site $i = L/2 + 1$ for the system size $L = 16$. For the block phase at $U/W = 4.0$ [Fig. 8(a)], a pseudogap with suppressed weight near the Fermi energy appears, which is in accord with the Lanczos DOS, suggesting a bad metallic behavior for the AF2 phase. In Fig. 8(b), results for the LDOS at the AF3 phase using $U/W = 9.1$ are shown. Here, due to the appearance of orbital-selective density order, we calculate results for two sites (one of each kind, i.e., with $\gamma = 3$ equal to 2.0 and 1.5) and then average to obtain a net LDOS. The resulting LDOS at $U/W = 9.1$ in Fig. 8(b) indicates the insulating behavior of the system.

In addition to the DOS, we have also investigated the charge fluctuations δN to distinguish between a metal and an insulator. Figure 8(c) displays the δN charge fluctuations defined as $\delta N = 1/L \sum_i (\langle n_i^2 \rangle - \langle n_i \rangle^2)$ (where $n_i = \sum_\gamma n_{i\gamma}$) and also the orbital-resolved charge fluctuation $\delta N_\gamma = \frac{1}{L} \sum_i \langle n_{\gamma,i}^2 \rangle - \langle n_{\gamma,i} \rangle^2$ varying U/W. For $U/W \lesssim 0.8$, the large local charge fluctuations indicate strong metallic behavior in the PM phase as expected. Increasing U/W, the charge fluctuations δN decrease substantially but remain finite
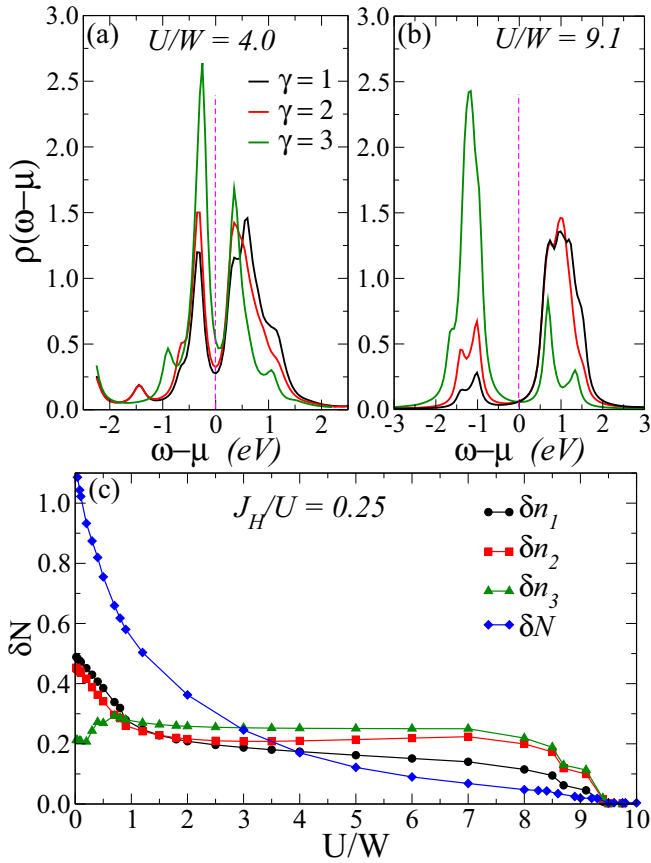
FIG. 8. Local DOS of different orbitals corresponding to different phases at $J_H/U = 0.25$ for system size $L = 16$ using dynamical DMRG. (a) The AF2 phase at $U/W = 4.0$ and (b) the AF3 phase at $U/W = 9.1$. (c) Site-averaged local charge fluctuations and orbital-resolved charge fluctuations vs U/W at $J_H/U = 0.25$ and for $L = 16$. The nonzero values indicate charge fluctuations are present in the entire AF2 phase, suggesting it is metallic.

for $U/W \lesssim 8.5$, hinting towards a (bad) metallic behavior of the system in the block AF2 phase. Moving beyond $U/W > 9.5$, the charge fluctuations approach zero, providing further evidence of insulating behavior in the AF1 phase. The AF3 phase is difficult to judge because of its narrow-range nature, but it also seems insulating. These results are in agreement with the Lanczos DOS analysis in Fig. 7.

B. Phase diagram varying J_H/U and U/W

Figure 9 contains the phase diagrams of our three-orbital Hubbard model using realistic hopping parameters for Na_2FeSe_2 and varying J_H/U from 0.15 to 0.30 and U/W from 0 to 10. The phase diagram shown in Fig. 9(a) is based on the DMRG calculations ($L = 16$), while Fig. 9(b) is based on Lanczos calculations using $L = 4$ sites. To obtain the phase boundaries among the different phases, we have used the peak values of the spin-structure factor $S(q_p)$ and the site-average occupancies of each of the orbitals $n_\gamma = \frac{1}{L} \sum_{i,\sigma} \langle n_{i\sigma\gamma} \rangle$. For lower values of U/W, as expected the metallic PM phase dominates in the phase diagram for any values of J_H/U. The phase boundary of the PM phase clearly is very similar between the
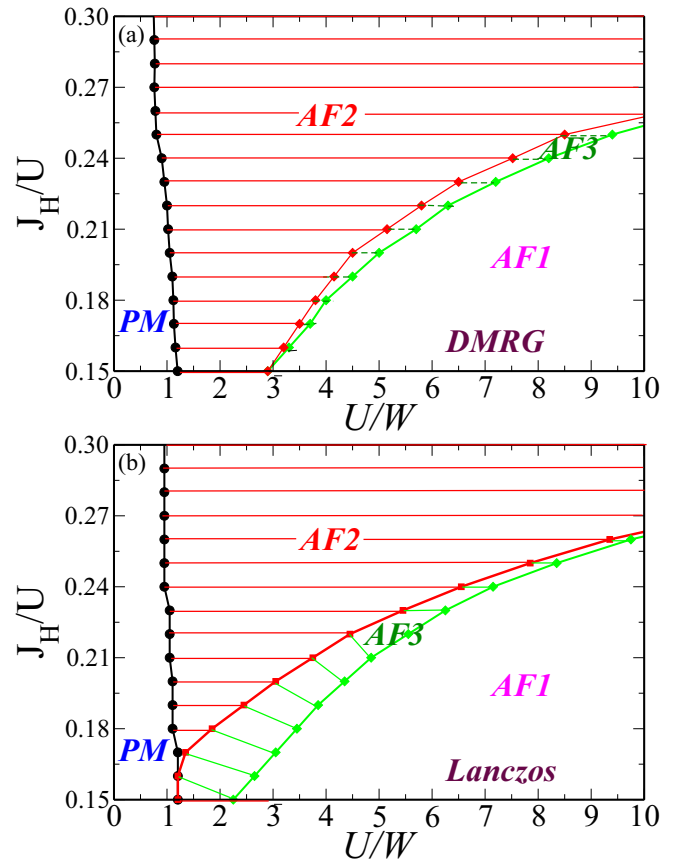
FIG. 9. Phase diagram of the three-orbital Hubbard model with the hopping amplitudes of Na_2FeSe_2, varying the Hund coupling and Hubbard interactions. Panel (a) depicts results based on DMRG, while panel (b) are results using the Lanczos method on an $L = 4$ sites cluster and open boundary conditions. PM stands for paramagnetic phase, while AF2 for block phase with ↑↑↓↓ order. The intermediate phase AF3 with ↑↑↓↑↓↓↑↓ spin ordering appears using both methods in a narrow range of couplings. AF1 stands for the staggered antiferromagnetic phase ↑↓↑↓↑.

DMRG and Lanczos results. Further increasing the Hubbard interaction U/W, in the lower range of Hund couplings J_H/U shown, the block AF2 phase stabilizes in a small region of the phase diagram, while the staggered AF1 phase dominates over a larger portion. At not too large J_H/U, the superexchange mechanism dominates and promotes primarily staggered AF1 magnetic ordering, as expected. For these moderate values of J_H/U, a rapid cascade of transitions (PM → AF2 → AF3 → AF1) is observed. For $J_H/U < 0.19$, the narrow region in between AF2 → AF1 shows incommensurate behavior (not shown), while for $J_H/U > 0.19$ this intermediate region displays the exotic AF3 spin order with peak at $q = 3\pi/4$.

Interestingly, by increasing J_H/U the block AF2 phase with spin configuration ↑↑↓↓ stabilizes over a large portion of the phase diagram. This magnetic block state (AF2) is the same as found before in the context of orbital-selective Mott phases [14,22,23], although here the three orbitals remain itinerant, i.e., none has a population locked to one. As in those previous efforts, we believe the block spin order AF2 arises from competing superexchange order at small J_H and
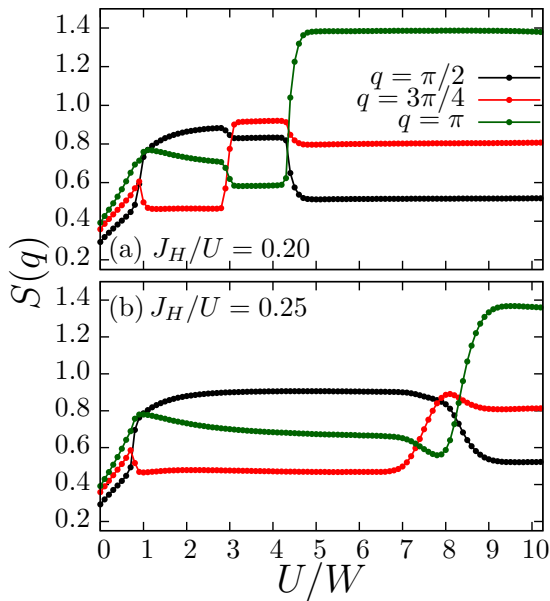
FIG. 10. Spin structure factors $S(q)$ at $q = \pi/2$, $3\pi/4$, and π vs U/W for (a) $J_H/U = 0.20$ and (b) $J_H/U = 0.25$, using the Lanczos method for $L = 4$ sites, and the three-orbital Hubbard model used here.

double-exchange ferromagnetism at large J_H. While in our phase diagram there is no ferromagnetic phase in the range studied, we found that removing the NNN hopping leads to a stable ferromagnetic region, as in previous efforts [14,22,23]. Thus the ferromagnetic state is certainly close in energy.

Also note the good agreement between the DMRG and Lanczos results found for the phase diagrams, see Fig. 9(a) vs Fig. 9(b), except for small J_H/U where the AF3 phase is broader with Lanczos than DMRG, with opposite effects for the AF2 region. This small difference may be due to size effects. However, at moderate J_H/U between 0.19 and 0.25— a region considered realistic for iron-based compounds—the AF2 phase, which represents our main prediction for the physics of Na$_2$FeSe$_2$ if ever synthesized, is large and robust as Fig. 5(a) shows using DMRG and Fig. 10(b) using Lanczos.

V. CONCLUSIONS

In this publication the phase diagram of the one-dimensional chain compound Na$_2$FeSe$_2$ has been

investigated. We used a realistic three-orbital Hubbard model with the hopping amplitudes derived from *ab initio* calculations. The phase diagram presented here was constructed at electronic density $n = 4$ per site (the analog of $n = 6$ in a five-orbital system). This is an interesting material of the family of iron superconductors that has both a dominant chain geometry in the structure (not ladder) and valence Fe^{2+}. Our phase diagram is based primarily on DMRG measurements of the orbital occupancy and spin structure factor, supplemented by Lanczos techniques. In comparison to previously studied $n = 5$ one-dimensional three-orbital models for iron-based compounds such as TlFeSe$_2$, which display a trivial staggered spin order, we find a much richer phase diagram for the alkali-metal iron selenide compound Na$_2$FeSe$_2$. In particular, at low J_H/U the staggered spin order dominates, but upon increasing J_H/U the block AF2 phase $\uparrow\uparrow\downarrow\downarrow$ is stabilized over a large region of the phase diagram. We also observed a narrow region of a new phase AF3, with charge density wave properties and a combination of features of the AF1 and AF2 dominant phases, leading to a net $\uparrow\uparrow\downarrow\uparrow\downarrow\downarrow\uparrow\downarrow$ magnetic order. Previous results with iron ladders suggest that high-pressure probes may also bring surprises, such as metallicity and even superconductivity. As a consequence, we encourage experimentalists to synthesize Na$_2$FeSe$_2$ and investigate its magnetic properties via neutron-scattering experiments.

[1] R. M. Fernandes and A. V. Chubukov, Rep. Prog. Phys. **80**, 014503 (2017).

[2] P. Dai, J. Hu, and E. Dagotto, Nat. Phys. **8**, 709 (2012).

[3] E. Dagotto, Rev. Mod. Phys. **85**, 849 (2013).

[4] T.-M. Chuang, M. P. Allan, Jinho Lee, Yang Xie, Ni Ni, S. L. Bud'ko, G. S. Boebinger, P. C. Canfield, and J. C. Davis, Science **327**, 181 (2010).

[5] H. Gretarsson, A. Lupascu, Jungho Kim, D. Casa, T. Gog, W. Wu, S. R. Julian, Z. J. Xu, J. S. Wen, G. D. Gu, R. H. Yuan, Z. G. Chen, N.-L. Wang, S. Khim, K. H. Kim, M. Ishikado, I. Jarrige, S. Shamoto, J.-H. Chu, I. R. Fisher, and Y.-J. Kim, Phys. Rev. B **84**, 100509(R) (2011).

[6] B. Wei, H. Qing-Zhen, C. Gen-Fu, M. A. Green, W. Du-Ming, H. Jun-Ba, and Q. Yi-Ming, Chin. Phys. Lett. **28**, 086104 (2011).

[7] E. Dagotto, J. Riera, and D. Scalapino, Phys. Rev. B **45**, 5744(R) (1992).

[8] E. Dagotto and T. M. Rice, Science **271**, 618 (1996).

[9] M. Mourigal, Shan Wu, M. B. Stone, J. R. Neilson, J. M. Caron, T. M. McQueen, and C. L. Broholm, Phys. Rev. Lett. **115**, 047401 (2015).

[10] J. M. Caron, J. R. Neilson, D. C. Miller, K. Arpino, A. Llobet, and T. M. McQueen, Phys. Rev. B **85**, 180405(R) (2012).

[11] J. M. Caron, J. R. Neilson, D. C. Miller, A. Llobet, and T. M. McQueen, Phys. Rev. B **84**, 180409(R) (2011).

[12] M. Wang, M. Yi, S. Jin, H. Jiang, Y. Song, H. Luo, A. D. Christianson, C. de la Cruz, E. Bourret-Courchesne, D.-X. Yao, D. H. Lee, and R. J. Birgeneau, Phys. Rev. B **94**, 041111(R) (2016).

[13] H. Lei, H. Ryu, A. I. Frenkel, and C. Petrovic, Phys. Rev. B **84**, 214511 (2011).

[14] J. Rincón, A. Moreo, G. Alvarez, and E. Dagotto, Phys. Rev. Lett. **112**, 106405 (2014).

[15] J. Rincón, A. Moreo, G. Alvarez, and E. Dagotto, Phys. Rev. B **90**, 241105(R) (2014).

[16] W. Bronger, A. Kyas, and P. Muller, J. Solid State Chem. **70**, 262 (1987).

[17] Z. Seidov, H.-A. Krug von Nidda, J. Hemberger, A. Loidl, G. Sultanov, E. Kerimova, and A. Panfilov, Phys. Rev. B **65**, 014433 (2001).

[18] R. G. Veliyev, Semiconductors **45**, 158 (2011).

[19] D. Welz and M. Nishi, Phys. Rev. B **45**, 9806 (1992).

[20] N. D. Patel, A. Nocera, G. Alvarez, A. Moreo, and E. Dagotto, Phys. Rev. B **96**, 024520 (2017).

[21] N. D. Patel, N. Kaushal, A. Nocera, G. Alvarez, and E. Dagotto, npj Quantum Mater. **5**, 27 (2020).

[22] J. Herbrych, J. Heverhagen, N. D. Patel, G. Alvarez, M. Daghofer, A. Moreo, and E. Dagotto, Phys. Rev. Lett. **123**, 027203 (2019).

[23] J. Herbrych, N. Kaushal, A. Nocera, G. Alvarez, A. Moreo, and E. Dagotto, Nat. Commun. **9**, 3736 (2018).

[24] N. D. Patel, A. Nocera, G. Alvarez, A. Moreo, S. Johnston, and E. Dagotto, Commun. Phys. **2**, 64 (2019).

[25] S. R. White, Phys. Rev. Lett. **69**, 2863 (1992).

[26] S. R. White, Phys. Rev. B **48**, 10345 (1993).

[27] H. Takahashi, A. Sugimoto, Y. Nambu, T. Yamauchi, Y. Hirata, T. Kawakami, M. Avdeev, K. Matsubayashi, F. Du, C. Kawashima, H. Soeda, S. Nakano, Y. Uwatoko, Y. Ueda, T. J. Sato, and K. Ohgushi, Nat. Mater. **14**, 1008 (2015).

[28] T. Yamauchi, Y. Hirata, Y. Ueda, and K. Ohgushi, Phys. Rev. Lett. **115**, 246402 (2015).

[29] For pairing in Se-based ladders, see J. Ying, H. Lei, C. Petrovic, Y. Xiao, and V. V. Struzhkin, Phys. Rev. B **95**, 241109 (2017).

[30] N. D. Patel, A. Nocera, G. Alvarez, R. Arita, A. Moreo, and E. Dagotto, Phys. Rev. B **94**, 075119 (2016).

[31] M.-T. Suzuki, R. Arita, and H. Ikeda, Phys. Rev. B **92**, 085116 (2015).

[32] Y. Zhang, L.-F. Lin, J.-J. Zhang, E. Dagotto, and S. Dong, Phys. Rev. B **95**, 115154 (2017).

[33] Y. Zhang, L.-F. Lin, J.-J. Zhang, E. Dagotto, and S. Dong, Phys. Rev. B **97**, 045119 (2018).

[34] S. Dong, J.-M. Liu, and E. Dagotto, Phys. Rev. Lett. **113**, 187204 (2014).

[35] Y. Zhang, L.-F. Lin, A. Moreo, S. Dong, and E. Dagotto, Phys. Rev. B **100**, 184419 (2019).

[36] Y. Zhang, L.-F. Lin, A. Moreo, S. Dong, and E. Dagotto, Phys. Rev. B **101**, 144417 (2020).

[37] Q. Luo, K. Foyevtsova, G. D. Samolyuk, F. Reboredo, and E. Dagotto, Phys. Rev. B **90**, 035128 (2014).

[38] Q. Luo, A. Nicholson, J. Rincón, S. Liang, J. Riera, G. Alvarez, L. Wang, W. Ku, G. D. Samolyuk, A. Moreo, and E. Dagotto, Phys. Rev. B **87**, 024404 (2013).

[39] J. Herbrych, J. Heverhagen, G. Alvarez, M. Daghofer, A. Moreo, and E. Dagotto, PNAS **117**, 16226 (2020).

[40] P. Stuble, S. Peschke, D. Johrendt, and C. Rohr, J. Solid State Chem. **258**, 416 (2018).

[41] J. P. Perdew, K. Burke, and M. Ernzerhof, Phys. Rev. Lett. **77**, 3865 (1996).

[42] P. E. Blöchl, Phys. Rev. B **50**, 17953 (1994).

[43] G. Kresse and J. Furthmüller, Phys. Rev. B **54**, 11169 (1996).

[44] G. Kresse and D. Joubert, Phys. Rev. B **59**, 1758 (1999).

[45] N. Marzari and D. Vanderbilt, Phys. Rev. B **56**, 12847 (1997).

[46] A. A. Mosto, J. R. Yates, Y. S. Lee, I. Souza, D. Vanderbilt, and N. Marzari, Comput. Phys. Commun. **178**, 685 (2007).

[47] R. Arita, H. Ikeda, S. Sakai, and M.-T. Suzuki, Phys. Rev. B **92**, 054515 (2015).

[48] K. Kuroki, S. Onari, R. Arita, H. Usui, Y. Tanaka, H. Kontani, and H. Aoki, Phys. Rev. Lett. **101**, 087004 (2008).

[49] G. Alvarez, Comput. Phys. Commun. **180**, 1572 (2009).

[50] Q. Luo, G. Martins, D.-X. Yao, M. Daghofer, R. Yu, A. Moreo, and E. Dagotto, Phys. Rev. B **82**, 104508 (2010).

[51] E. Dagotto, T. Hotta, and A. Moreo, Phys. Rep. **344**, 1 (2001).

[52] A. Nocera and G. Alvarez, Phys. Rev. E **94**, 053308 (2016).